

1 Generative AI for image reconstruction in Intensity Interferometry: a first attempt

2 KM NITU RAI,^{1,2} YURI VAN DER BURG,³ SOUMEN BASAK,¹ PRASENJIT SAHA,³ AND SUBRATA SARANGI^{4,5}

3 ¹*School of Physics, Indian Institute of Science Education and Research Thiruvananthapuram, Maruthamala PO, Vithura,*
4 *Thiruvananthapuram 695551, Kerala, India.*

5 ²*Aryabhatta Research Institute of Observational Sciences, Manora Peak, Nainital 263129, India.*

6 ³*Physik-Institut, University of Zurich, Winterthurerstrasse 190, 8057 Zurich, Switzerland.*

7 ⁴*School of Applied Sciences, Centurion University of Technology and Management, Odisha-752050, India.*

8 ⁵*Visiting Associate, Inter-University Centre for Astronomy and Astrophysics, Post Bag 4, Ganeshkhind, Pune 411 007, Maharashtra,*
9 *India.*

ABSTRACT

In the last few years Intensity Interferometry (II) has made significant strides in achieving high-precision resolution of stellar objects at optical wavelengths. Despite these advancements, phase retrieval remains a major challenge due to the nature of photon correlation. This paper explores the application of a conditional Generative Adversarial Network (cGAN) to tackle the problem of image reconstruction in II. This method successfully reconstructs the shape, size, and brightness distribution of simulated, fast-rotating stars based on a sparsely sampled spatial power spectrum obtained from a hypothetical ground-based II facility composed of four Imaging Atmospheric Cherenkov Telescopes (IACTs). Although this particular example could also be addressed using parameter fitting, the results suggest that with larger arrays much more complicated systems could be reconstructed by applying machine-learning techniques to II.

1. INTRODUCTION

Humans instinctively feel a relationship with the stars. One of the primary scientific projects of humanity is to figure out what the stars are and how do they do what they do. The first obvious step in this project, beyond measuring their global parameters like diameter, mass, orbital and astrometric elements, is to obtain images of the stars with all details of the stellar surfaces. In case of the Sun, this is done routinely by observatories and sun-observation satellites. But such routine still remains a challenge even for the α -centauri system, our nearest stellar neighbour. The objective is to achieve capability of high fidelity image reconstruction of distant stars. Two interferometry based techniques, namely, Michelson Interferometry (MI) or Intensity Interferometry (II) have emerged during the last century to address this objective. A discussion of the development of these two approaches and comparison of their respective merits and challenges can be found in (?). The work reported here presents the results of a first effort at applying a Conditional Generative Adversarial (neural) Network (cGAN) to image reconstruction of a fast rotator using its simulated II observations.

The foundational basis of II stems from the pioneering experiments and theoretical investigations, widely referred to as the “HBT effect”, carried out initially by

Hanbury Brown and Twiss (HBT) ??? and, later, by Glauber (?). The correlation between photons (called HBT effect) measured by a pair of photon detectors in two coherent beams of light was reported in 1956 ?. ? present a modern-day variant of this experiment, carried out with pseudo-thermal light. The HBT Effect and the related theoretical investigations laid the foundation for the modern field of Quantum Optics.

Hanbury Brown and his collaborators led the creation and installation of the iconic II facility at Narrabri, Australia and reported the measurement of angular diameters of 32 stars and a few multiple star-systems (?). Soon after this work, however, II observations of stars was stalled for over four decades due to the limits of the then available photon detectors and data processing equipment. With gradual mitigation of such issues, proposals to utilize Imaging Atmospheric Cherenkov Telescope (IACT) facilities for conducting II observations of stars have emerged(????) as a secondary science application of these facilities during moonlit nights. SII observations at VERITAS, MAGIC, and HESS are now being reported (e.g., ???). This approach has the potential to enhance the scientific output of existing IACT facilities, and especially of the upcoming Cherenkov Telescope Array Observatory (CTAO). Simulations carried out by Rai et al. (??, e.g.,) have shown that recent advance-

72 movements in photon detectors could be effective in achieving
 73 high-precision measurements of parameters for stellar
 74 objects.

75 The thrust of these efforts has been to measure the
 76 average global parameters of stars and star systems.
 77 The high fidelity imagery, however, would transcend the
 78 measurement of global and average stellar parameters,
 79 such as angular diameters, binary separations, and orbital
 80 characteristics, which offer only an integrated view
 81 of the star or star system as a whole. Such imaging capabilities
 82 promise direct insights into the dynamic surface phenomena,
 83 including limb darkening, convection cells, granulation,
 84 star spots, oblateness and gravity darkening in rapid rotators
 85 and atmospheric structures, akin to the detailed observations
 86 routinely conducted on our own Sun.

88 As it stands today, studies grappling various issues
 89 of image reconstruction are being reported (????).
 90 MI-based image reconstruction has made substantial
 91 progress in this area with efforts at generating constructed
 92 images of stars like Betelgeuse (?) and AZ Cyg (?). On the other hand, II-based methods are
 93 in a nascent stage. The recent publications ?? have
 94 demonstrated, through outdoor experiments, imaging
 95 millimeter-scale targets at 1.36 km with a resolution 14
 96 times better than a single telescope's diffraction limit. A
 97 "flexible computational algorithm" reconstructs images
 98 from intensity correlations, overcoming atmospheric turbulence
 99 and optical imperfections.

100 We report here, the results of our attempt – the first of
 101 its kind – to construct the gravity-darkened sky-image
 102 of fast rotating stars consistent with their respective
 103 simulated ground-based II-observations using a cGAN
 104 neural network architecture. Image reconstruction in
 105 gravity darkened fast rotating stars has long been examined
 106 using various methods in MI (?????????). Recently
 107 photosphere oblateness of γ -Cassiopeia (?) has
 108 been measured at the VERITAS observatory using II.
 109 These results, and especially, that by ? put our work
 110 in context. Thus our work presented here is a natural
 111 next step of the work of Archer et al and others. We
 112 emulate the cGAN model ? to reconstruct images of
 113 fast-rotating stars using their simulated Intensity Interferograms
 114 and sky-intensity distributions as input data
 115 for training, testing, and validation. We consider an
 116 array of four Imaging Cherenkov Telescopes (IACTs)
 117 whose relative positions approximately mimic those at
 118 VERITAS and simulate observations of a set of synthetically
 119 generated fast-rotating stars. The image predicted by the trained cGAN shows promising results in
 120 reconstructing the stars' shapes and sizes. The recon-

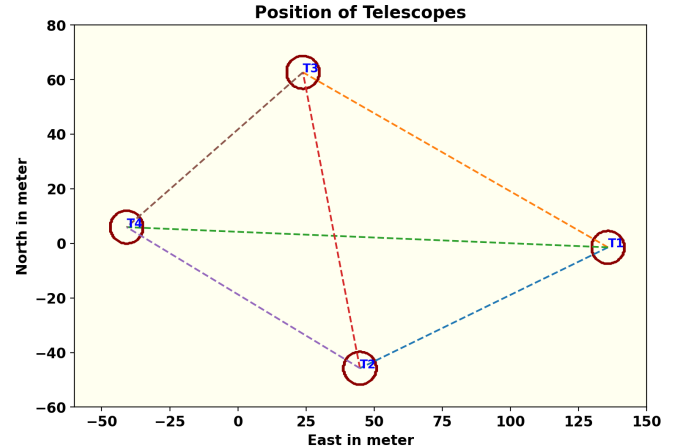


Figure 1. A schematic representation of a hypothetical observation facility with an array of four Cherenkov Telescopes (IACTs) whose relative positions approximately mimic those at VERITAS. This array is used in simulating the II observation of the fast rotators. Each of the telescopes has a diameter of 12m. The baselines provided by the array are of the order of 100m.

123 structured brightness distributions are then assessed using
 124 moments.

125 This paper is organized as follows. The next section
 126 discusses briefly the past efforts at image reconstruc-
 127 tion on II, followed by the section on a discussion of II,
 128 focusing on its signal and noise characteristics for fast-
 129 rotating stars along the Earth's rotation. The following
 130 section introduces the cGAN formulation and its struc-
 131 ture. The fifth section details the parameter selection
 132 for training the network for image reconstruction. The
 133 sixth section presents the results of the trained network
 134 both visually and via image moments. Finally, the pa-
 135 per concludes with a discussion of the overall results.

138 2. PAST EFFORTS AT IMAGE 139 RECONSTRUCTION IN INTENSITY 140 INTERFEROMETRY

141 Several approaches have been developed for phase re-
 142 construction in intensity interferometry (II). ? intro-
 143 duced triple-intensity correlation, applied by ? to micro-
 144 scopic systems and extended by ??? to measure stellar
 145 diameters and phases, though limited by low signal-to-
 146 noise ratio (SNR). ? proposed an iterative phase re-
 147 trieval method using image and diffraction plane data,
 148 sensitive to initial estimates and convergence speed. ?
 149 improved this with the Hybrid Input-Output algorithm,
 150 enhancing robustness in noisy conditions. ? utilized
 151 Cauchy-Riemann relations for 1-D and 2-D image recon-
 152 struction, applied to simulated stellar data with Imag-
 153 ing Cherenkov Telescope Arrays (??), but faced com-

putational complexity for higher dimensions. ? introduced a regularized iterative method incorporating priors (e.g., sparsity) to mitigate noise and ill-posedness, though challenged by parameter tuning and initial guess sensitivity. The Transport-of-Intensity Equation (TIE), proposed by ?, retrieves phase from intensity variations across planes; ? solved TIE as a Poisson equation using a maximum intensity assumption, while ? combined TIE with the Transport of Phase Equation for improved accuracy across arbitrary apertures and non-uniform illumination, with convergence dependent on initial guesses and boundary conditions.

With non-linearity built into their architecture, artificial neural networks (ANNs) empowered by deep learning methods are promising for exploring the task of reconstructing images of stellar objects from ground-based observations. Convolutional Neural Networks (CNNs), with their specialized architecture for processing two-dimensional datasets, are a natural choice for image processing tasks. In astronomical image reconstruction projects, a common challenge is that the interferometric data are typically undersampled as well as noisy. Therefore, the CNN architectures and deep learning methods employed must be capable of reliably learning both the global context of the training dataset and the local features within it. Among the various CNN architectures, U-Net models (?) have proven successful in such tasks.

Furthermore, given that achieving a high signal-to-noise ratio (SNR) is often challenging in astronomical datasets, it is immensely beneficial if additional data can be generated using the available information from the observed sky density distribution and ground-based observations (II data, in our case) of the sources under investigation. Generative Adversarial Networks (GANs), introduced by ?, have been successful in such data augmentation tasks. Conditional GAN (cGAN) architectures, proposed by ? and applied to a wide variety of datasets by ?, leverage additional information about the images in the training datasets and have demonstrated remarkable robustness in image recovery across diverse data types.

In the astrophysical context, ? employed a GAN model to recover features, such as spiral arms, central bulges, and disk structures of galaxies, from noise-affected images. ? developed and customized a Deep Convolutional GAN, dubbed “CosmoGAN”, capable of generating high-fidelity weak-lensing convergence maps of dark matter distribution that statistically reproduce real weak lensing structures. ? have successfully generated credible images of planets, nebulae, and galaxies using “lightweight” and “physics-uninformed” GANs to produce synthetic images of celestial bodies. They

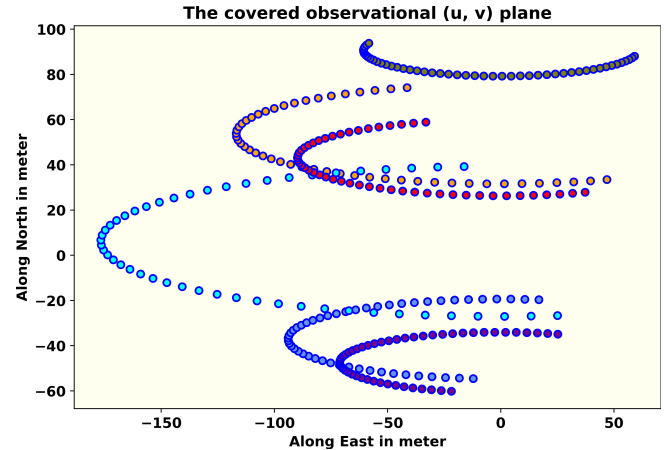


Figure 2. The tracks of the baselines due to Earth rotation (described in sec. 3.3) provided by the hypothetical observation facility of four telescopes arranged in fig. 1 for one night of observation. The number of baselines scales as square of number of telescopes in the array thus leading to greater coverage of the observational plane and better image reconstruction prospects.

also generated a “Hubble Deep Field-inspired” wide-view simulation of the universe.

3. INTENSITY INTERFEROMETRY (II) WITH IACT ARRAYS

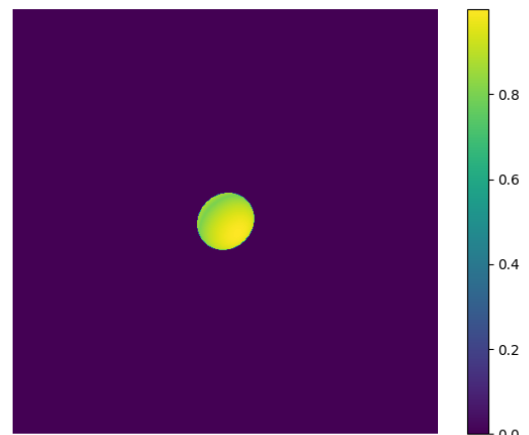


Figure 3. This figure shows one of the simulated fast rotating stars (FRS). The brightness is highest at the poles; gravity darkening visible along the equator. A total of 31460 such images of FRS with different parameter values have been generated to train the model.

This section presents a brief conceptual overview of how an array of telescopes is used to perform II observations, and explains the Signal-to-Noise Ratio (SNR) from these measurements.

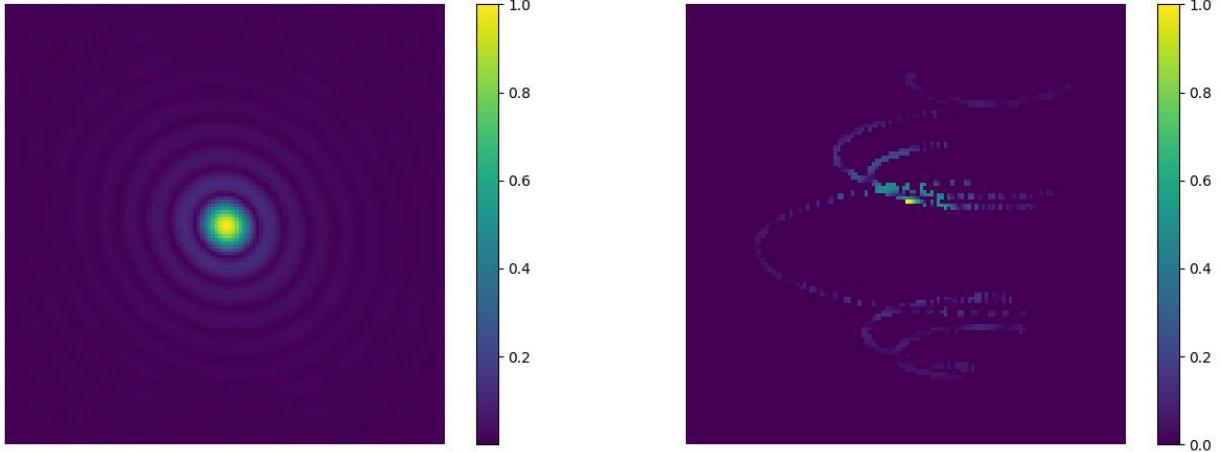


Figure 4. The left panel shows the absolute value of the two-dimensional Fast Fourier Transform of the source depicted in Fig. 3. It represents the intensity interferometric (u, v) plane image of the source that would be obtained by an infinite number of baselines (or an infinite number of telescopes observing the source). The right panel shows the absolute value of the same source measured along the tracks shown in Fig. 2. This figure reflects the sparse nature of the signal received by a realistic finite number of telescopes and baselines sampled from the full (u, v) plane signal space, as shown in the figure on the left panel. Both figures are plotted on a linear scale and normalized to the maximum pixel value in each respective figure.

3.1. The signal for II

As a simple example, let us consider a pair of IACTs pointed at a star. Suppose the two telescopes simultaneously measure the intensity of radiation $I_1(t)$ and $I_2(t)$, respectively. The signals from these detectors are cross-correlated and averaged over time, yielding the second order ($n = 2$) correlation of these intensities as (cf. ??)

$$g^{(2)} = \frac{\langle I_1(t) \cdot I_2(t + \tau) \rangle}{\langle I_1(t) \cdot \langle I_2(t) \rangle \rangle} \quad (1)$$

where τ is the time delay between the telescopes. For spatially coherent and randomly polarized light, Eq. (1) reduces to the relation (sometimes called the Siegert relation, see e.g., ?).

$$g^{(2)} = 1 + \frac{\Delta f}{\Delta \nu} |V_{12}|^2 \quad (2)$$

where Δf is the electronic bandwidth of the photon detectors which measure the intensities and $\Delta \nu$ is the frequency bandwidth of the filters employed in the telescopes to observe the star. Values of $\Delta \nu \sim 1$ THz and $\Delta f \sim 1$ GHz are typical of recent work. In Eq. (2), V_{12} , referred to as the complex visibility function, is the Fourier transform of the source brightness distribution. It contains information about the star's angular diameter. However, the phase information is lost since we measure only the absolute value $|V_{12}|^2$. In observational astronomy, the correlation is often expressed in terms of the normalized contrast, given by:

$$c = g^{(2)} - 1 = \frac{\Delta f}{\Delta \nu} |V_{12}|^2 \quad (3)$$

with $|V_{12}|^2$ being a function of baseline $b = \sqrt{u^2 + v^2}$ on the observational plane (u, v). This implies the strength of the signal would be enhanced if a larger number of baselines or pairs of telescopes are employed.

3.2. The Signal-to-Noise Ratio for II

The primary purpose of IACTs is to study high-energy gamma rays (with energy $E \geq 30$ GeV) arriving from cosmic sources, entering the Earth's atmosphere, and initiating Cherenkov showers in the upper atmosphere due to multiple scattering. These telescopes feature an array of mirrors that focus light received from a sky source onto their respective set of photo-multiplier tubes (PMTs, see e.g., ?) with appropriate specifications needed for II observations. In the simulation model adopted here, we consider a set of four IACTs, each with similar properties. The positional configuration of these IACTs is shown in Fig. 1. The optical signal directed to a PMT is filtered using a spectral filter with a chosen mean observational wavelength λ and corresponding bandpass $\Delta \lambda$. The use of filters not only reduces background noise but also improves the signal quality and the efficiency of the PMTs. Filtering background sky-light becomes even more significant in II observations, as, currently, these are carried out during full moon nights when the primary function of the IACTs (of observing Cherenkov Showers) is rendered infeasible. It is important to note that the light from the stellar source is focused on a PMT attached with each of the telescopes during II observations.

The significance of the signal can be expressed in terms of the signal-to-noise ratio (SNR), which depends on many factors. However, most importantly, it does not depend on the optical bandwidth $\Delta\nu$ of the radiation for a two-telescope correlation. The explanation for the independence of the SNR from $\Delta\nu$ is provided in several works (e.g., subsection 4.1 of ?). The Signal-to-Noise is given by

$$SNR = A \cdot \alpha \cdot q \cdot n \cdot F^{-1} \cdot \sigma \cdot \sqrt{\frac{T\Delta f}{2}} \cdot |V_{12}|^2 \quad (4)$$

Here, A is the total mirror area, α is the quantum efficiency of the PMTs, q is the throughput of the remaining optics, and n is the differential photon flux from the source. The excess noise factor of the PMTs is represented by F , T denotes the observation time, and σ is the normalized spectral distribution of the light (including filters) (e.g., ?).

3.3. Baseline considerations

The measurement of the size of stellar objects via squared visibility depends on the distance between the telescopes, known as the baseline b .

$$|V_{12}(b)|^2 = \frac{c(b)}{c(0)} \quad (5)$$

For achieving a good SNR with a given telescope configuration, covering as much as possible of the interferometric plane is always desirable. If the source is at the zenith, the coordinates in the Fourier plane (u, v) are given by:

$$(u, v) = \frac{1}{\lambda} (b_E, b_N) \quad (6)$$

where b_E and b_N are, respectively, the baselines expressed in east and north coordinates. However, the sources can be anywhere on the sky, and the telescopes are stationary and may also have different relative altitudes b_A depending on the available terrain. In order to gather maximum possible information on the source during the observation session and to cover as much of the observational plane as possible during such sessions, Earth's rotation must be taken into account using rotated baselines. For a given stellar source with declination δ and hour-angle h , as observed by telescopes located at latitude l , equation (7) provides the rotated baselines for a given pair of telescopes (see e.g., eqs. 8–10 from ?) with the R -matrices representing the respective rotation operations.

$$\begin{pmatrix} u \\ v \\ w \end{pmatrix} = R_x(\delta) \cdot R_y(h) \cdot R_x(-l) \begin{pmatrix} b_E \\ b_N \\ b_A \end{pmatrix} \quad (7)$$

Fig. 2 shows the track of six baselines generated from the telescopes (Fig. 1) due to the Earth's rotation. Since every pair of telescopes traces an ellipse in the Fourier plane, the total number of ellipses scales as

$$\mathcal{N} = \frac{1}{2} N_T \cdot (N_T - 1) \quad (8)$$

where N_T is the number of telescopes considered. As the number of baselines increases non-linearly, Intensity Interferometry (II) benefits greatly from a large number of telescopes. The CTAO can offer many more baselines — ? considered the telescope configurations then being planned and showed how it would provide a dense coverage of the interference plane.

3.4. A Fictitious Fast Rotating Star: Our Test Case

In our work presented here, we attempt image reconstruction of a fast-rotating star using its simulated Intensity Interferometric observation in a cGAN architecture. Fast-rotating stars are important test cases for understanding various astrophysical processes, including stellar evolution, internal structure, and dynamical behaviour over time. Fast rotation causes stars to adopt an oblate shape, flattening at the poles and bulging at the equator due to the stronger centrifugal force (e.g., ??). Fig. 3 shows an image qualitatively representing a fictitious fast-rotating star, with brightness (and, therefore, the effective surface temperature) distributed across its surface. The brightness (effective temperature) is highest at the poles and lowest at the equator, a phenomenon known as gravity darkening (?). First direct interferometric detection of stellar photospheric oblateness (of Altair) was pioneered by van Belle et al. ? using the Palomar Testbed Interferometer (PTI) and the Navy Prototype Optical Interferometer (NPOI). Gravity darkening due to fast rotation was first observed through interferometric and spectroscopic data from the CHARA Array for the fast-rotating star Regulus (?). As pointed out earlier, these two pieces of work, all using Michelson Interferometry, make a subset of several others (?????????). The first observation of photospheric oblateness (of γ Cassiopeiae or γ -Cas) using Intensity Interferometry (II) has been recently carried out at VERITAS observatory and is reported by Archer et al. ?. Reportage of such observations of other γ -Cas like targets and other class of FRS by Cherenkov Telescope arrays, such as the MAGIC array, are expected by 2026. In addition, observation and measurement of gravity darkening using II is the natural next step and is yet to be reported. In this context, our work of reconstructing the image of FRSs from their II-simulated observations using cGAN is an attempt at solving this

362 inverse problem along with mitigation of loss of phase
 363 information in II.

364 II counts the photons arriving at the telescopes from
 365 the stellar object. The correlation of these photon
 366 arrivals at the telescopes yields the squared visibility
 367 Eq. (5), as explained in subsection 3.1. The left panel of
 368 fig. 4 shows the signal from the source shown in Fig. 3
 369 using II, displayed on linear scales. Point to note here
 370 is that this figure represents the signal from the source
 371 that would be recorded by an infinite number of base-
 372 lines provided by an infinite number of telescopes on
 373 the interferometric plane. In practice, only a small part
 374 of this information is available (as seen in right panel
 375 of Fig. 4), because one has a finite number of baselines
 376 corresponding to the finite number N_T of telescopes at
 377 our disposal and a limited observation schedule. We
 378 have simulated the II observation of the fictitious star
 379 by a hypothetical observation facility having an array of
 380 four IACTs with their relative positions approximating
 381 those at VERITAS (correlated with baselines as seen in
 382 Fig. 1) over one night. Using this modest amount of
 383 signal from one night's observation, we have trained a
 384 cGAN to construct the image of the source.

386 4. GENERATIVE ADVERSARIAL NETWORKS

387 Generative Adversarial Networks (GANs) were intro-
 388 duced by ?. A GAN model involves two competing deep
 389 neural network models, referred to as the Generator and
 390 the Discriminator. These two networks engage in a zero-
 391 sum “Minimax” game, as in the Game Theory. Given
 392 a real data set $\{x_i\}$ (for example, a set of real images)
 393 drawn from some unknown distribution $P_{\text{data}}(x)$ gen-
 394 erated by some unknown or ill-understood process, the
 395 objective here is to generate a new set (of images) whose
 396 probability distribution should match $P_{\text{data}}(x)$ as closely
 397 as possible. During the training of the two models, the
 398 Generator samples a latent variable z from a known
 399 prior distribution $P_z(z)$ (e.g., the Normal Distribution)
 400 and produces a synthetic sample $G(z)$ to start with and,
 401 subsequently, based on updates received from the Dis-
 402 criminator as its training progresses. The Discriminator,
 403 being a probabilistic binary classifier, receives either a
 404 real data sample x or a generated sample $G(z)$, and
 405 outputs a probability that the input is real. The Dis-
 406 criminator aims to maximise its classification accuracy,
 407 while the Generator aims to fool it by trying to minimize
 408 it. The training of these two networks proceeds alter-
 409 nately leading to the optimization of the adversarial loss
 410 function $L(D, G)$ given by

$$411 \begin{aligned} L(D, G) &= \min_G \max_D V(D, G) \\ &= \mathbb{E}_{x \sim p_{\text{data}}(x)} [\log D(x)] \\ &\quad + \mathbb{E}_{z \sim p_z(z)} [\log (1 - D(G(z)))] . \end{aligned} \quad (9)$$

412 The two neural networks $G(z) \equiv G(z; \theta_G)$ and $D(x) \equiv$
 413 $D(x; \theta_D)$ are parameterized by θ_i with $i = G$ or D re-
 414 spectively. During its training, the Generator gener-
 415 ates the differentiable function $x_{\text{gen}} \equiv G(z)$ that maps
 416 z to the data space x . Through such maps the Genera-
 417 tor generates its own distribution $p_G(x_{\text{gen}})$ and through
 418 the training episodes, specifically by iteratively updat-
 419 ing its parameters θ_G , aligns this distribution with the
 420 distribution of real data $p_{\text{data}}(x)$. The training data set
 421 provided to the Discriminator is constructed by mixing
 422 real data points x and generated data points x_{gen} in
 423 equal ratio. The Discriminator generates the function
 424 $D(x)$ that represents the probability that x originates
 425 from real data. Eq.(9) implies that training of the GAN
 426 model moves towards maximization of the expectation
 427 of $D(x)$. Through this process, both the parameters θ_G
 428 and θ_D are optimized such that $p_G(x_{\text{gen}})$ gets maximally
 429 aligned with $p_{\text{data}}(x)$.

430 For a given fixed Generator $G(z)$, the problem can be
 431 reformulated as:

$$432 \begin{aligned} \max_D V(D, G) &= \mathbb{E}_{x \sim p_{\text{data}}} [\log D_G^*(x)] \\ &\quad + \mathbb{E}_{x \sim p_G} [\log (1 - D_G^*(x))] \end{aligned} \quad (10)$$

433 where D_G^* denotes the optimum of the discriminator.
 434 As seen in equation (11), the global optimum of equation
 435 (10) is achieved if and only if $p_G = p_{\text{data}}$. Furthermore,
 436 if both G and D are allowed to reach their respective
 437 optima, – the so called Nash point of the Minimax game
 438 – p_G converges to p_{data} .

$$439 D_G^*(x) = \frac{p_{\text{data}}(x)}{p_{\text{data}}(x) + p_G(x_{\text{gen}})} \quad (11)$$

440 At this point, the Discriminator finds its job no better
 441 than random guessing. A more comprehensive discus-
 442 sion of the problem, including proofs, is provided in ?.

443 Subsequently, the GAN framework was extended to
 444 a conditional model (?). This new model, known as
 445 “conditional GAN” or cGAN injects a conditioning vari-
 446 able y into both networks: the Generator now generates
 447 $G(z | y)$, and the Discriminator evaluates $D(x | y)$. The
 448 adversarial objective becomes

$$449 \begin{aligned} V(D, G) &= \mathbb{E}_{x, y \sim p_{\text{data}}(x)} [\log D(x|y)] \\ &\quad + \mathbb{E}_{z, y \sim p_z(z)} [\log (1 - D(G(z|y)|y))] \end{aligned} \quad (12)$$

450 The conditional variable y in a cGAN can be various
 451 additional information including images, labels or text
 452 contextual to “ground truth” real data x . Among var-
 453 ious types of cGANs, Pix2Pix GAN with its image-to-
 454 image translation design is suitable for the task at hand.
 455 In our work, we specifically use this conditional variable

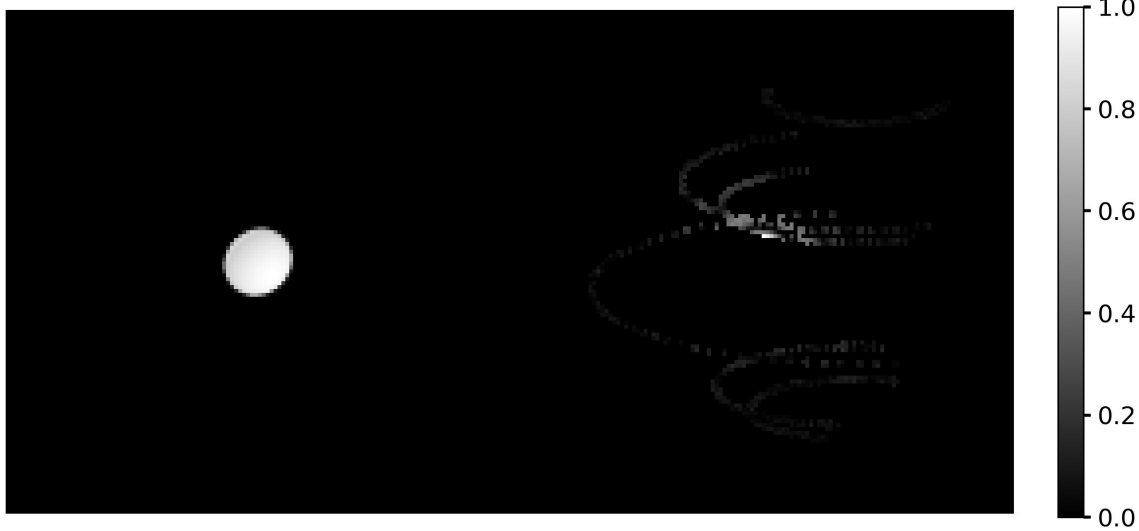


Figure 5. An illustrative example of the input used for training the cGAN model. The picture on the left shows the source image, which serves as the ground truth or the real data (x), as mentioned in the Flow Diagram (Fig. 6) discussed later during the training). The picture on the right represents the simulated II observation pattern of the source (on the left) using a hypothetical observation facility having as array of four IACTs (see Fig. 1) and the tracks of the six telescope baselines (see Fig. 2) generated by these four IACTs due to Earth’s rotation during the observation session. This pattern referred to as y , in the Flow Diagram (Fig. 6) discussed later) forms the “condition” during the training to which the GAN model has to conform. Salt-and-pepper noise is added to this pattern for enhancing the robustness of the cGAN model. Together, these images form a training pair, where the GAN learns to reconstruct a predicted image (modeling of observed signal) similar to ground truth (left) from the noisy baseline signal (right). The grayscale in both images is normalized to the brightest pixel.

456 by choosing y to represent the ground-based intensity-
 457 interferometry (II) observation patterns: the Generator
 458 is trained to produce stellar surface images that not
 459 only look realistic but also conform to the measured II
 460 correlations, while the Discriminator judges realism *and*
 461 consistency with the II data.

462 ? further observed that combining the cGAN from
 463 Eq. (12) with the traditional $L_1(G)$ loss (also known
 464 as the Mean Absolute Error) improves the results, as
 465 the Generator is encouraged to produce outputs closer
 466 to the target image in a pixel-wise sense. We adopt
 467 this approach in the training of our cGAN model by
 468 including $L_1(G)$ defined in eq.(13)

$$469 \quad L_1(G) = \mathbb{E}_{x \sim p_{\text{data}}, z \sim p_z(z)} [\|x - G(z | y)\|_1]. \quad (13)$$

470 The total adversarial loss function, along with the L_1
 471 loss modulated by a hyperparameter λ then becomes

$$472 \quad L_{\text{tot}} = \arg \min_G \max_D V(D, G) + \lambda \cdot L_1(G). \quad (14)$$

473 This type of network has demonstrated remarkable
 474 robustness across a variety of applications. For exam-
 475 ple, it can generate colored images from grayscale inputs
 476 based on architectural labels, transform images from day
 477 to night, and even predict maps from satellite data. A
 478 more extensive list of applications is provided in ?.

480

4.1. Generator

481 As discussed above, in a GAN the Generator, a deep
 482 neural network in itsel, is responsible for producing
 483 synthetic data, in this case, images that resemble those
 484 of a fast-rotating star. In this work, the Generator is im-
 485 plemented as a U-Net convolutional network (?). The
 486 U-Net consists of a symmetric encoder-decoder struc-
 487 ture forming a characteristic “U” shape along with skip
 488 connections: the left (contracting or down-sampling)
 489 path, the right (expanding or up-sampling path) and the
 490 connecting (bottle-neck) path. The left down-sampling
 491 path repeatedly applies 3×3 convolutions (padded to
 492 preserve spatial dimensions) followed by LeakyReLU ac-
 493 tivations and strided convolution (with stride of 2), by
 494 progressively halving the spatial resolution while dou-
 495 bling the channel depth (typically $64 \rightarrow 128 \rightarrow 256 \rightarrow$
 496 $512 \rightarrow 1024$). At the bottleneck, high-level features
 497 are processed without further spatial reduction. The
 498 right up-sampling path mirrors this process using 2×2
 499 transposed convolutions (stride 2) for up-sampling, halv-
 500 ing the channel count at each level and using ReLU
 501 as the activation function for all its layers except the
 502 output layer. Additionally, a dropout layer is intro-
 503 duced at the beginning of the upsampling phase to mit-
 504 iate overfitting of the Generator model (?). Critically,
 505 long skip connections concatenate feature maps from

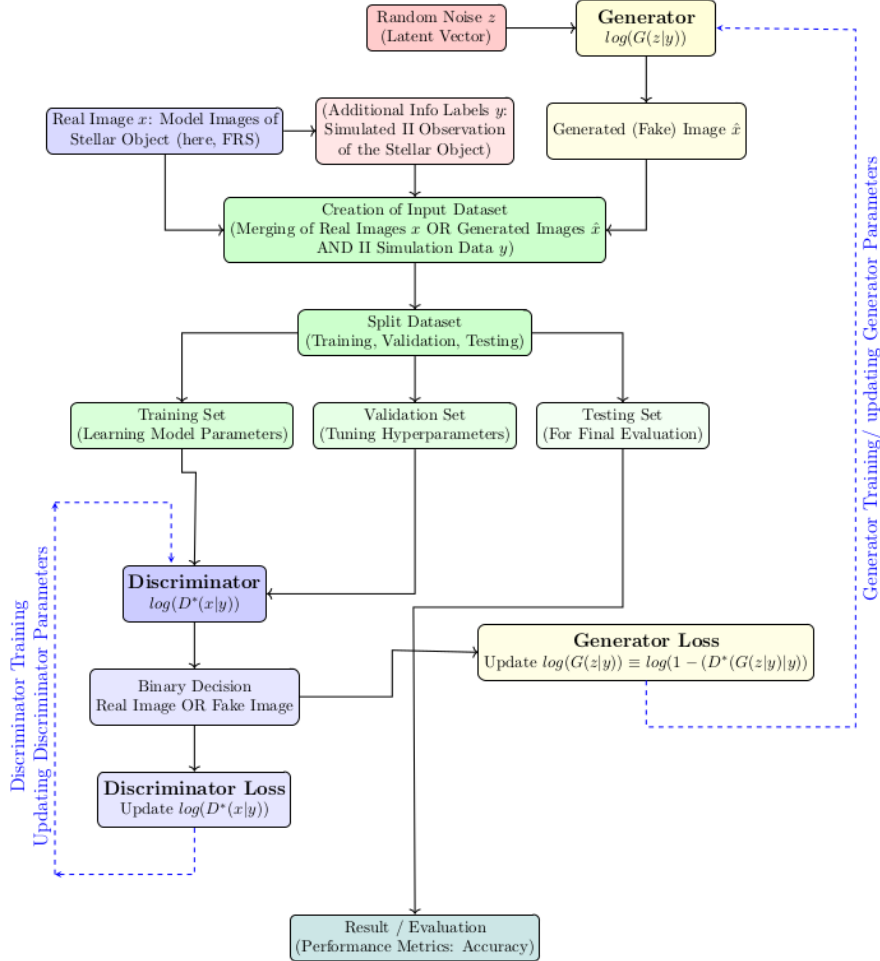


Figure 6. A schematic representation of the features of a cGAN model used in this work and the iterative process of its training, validation and testing. The process constitutes four broad stages: (1) choice of an appropriate GAN architecture including both the Discriminator and the Generator (not shown in this figure) (2) preparation of the Training, Validation and Testing datasets and (3) Training and Validation of the Model (4) Testing and Evaluation of the Model. The stages (2), (3) and (4) are depicted in this figure. The datasets are prepared in three broad steps: (i) generating the “ground truth” images of fictitious fast-rotators x , the sparse II images y used as the “condition” images in the Model and the generated images z sampled from a Normal Distribution (ii)merging these images into individual files with $(x|y)$ and/or $(z|y)$ (as seen in an illustrated sample in Fig.(5)) and generating the full dataset in this process, and finally (iii) partitioning the full dataset into Training Set, Validation Set and the Testing Set. After the iterative training of the Model and its validation process is complete (“Nash point” of the Minimax Game is reached), the Model is tested using the Testing Set and evaluated.

each encoder (down-sampling) level to the corresponding decoder (up-sampling level), directly injecting high-resolution details into the reconstruction process. This enables the network to “remember where everything is” while the deep bottleneck still provides the large receptive field needed to think globally about image structure and semantics. Besides the strided convolutions, modern variants of U-Nets used in state-of-the-art GANs incorporate residual blocks within resolution levels, and frequently add spectral normalization and self-attention at the bottleneck for improved training stability and

long-range dependency modelling. These architectural choices allow our U-Net generator to simultaneously recover sharp, high-frequency details (stellar limb edges, limb-darkening profiles, gravity darkening, and rapid-rotation-induced oblateness) and enforce global coherence (overall disk morphology and physical consistency with the observed interferometric visibilities)—making it ideally suited for high-fidelity sky-image reconstruction of fast-rotating stars from sparse ground-based intensity interferometry observations.

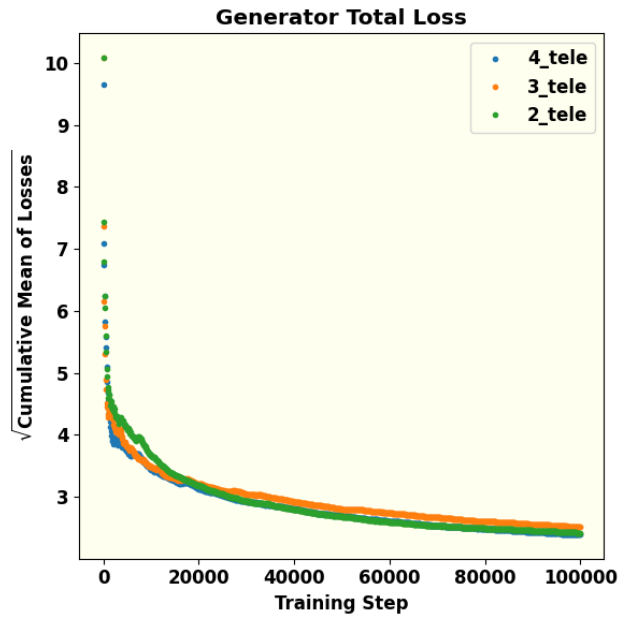
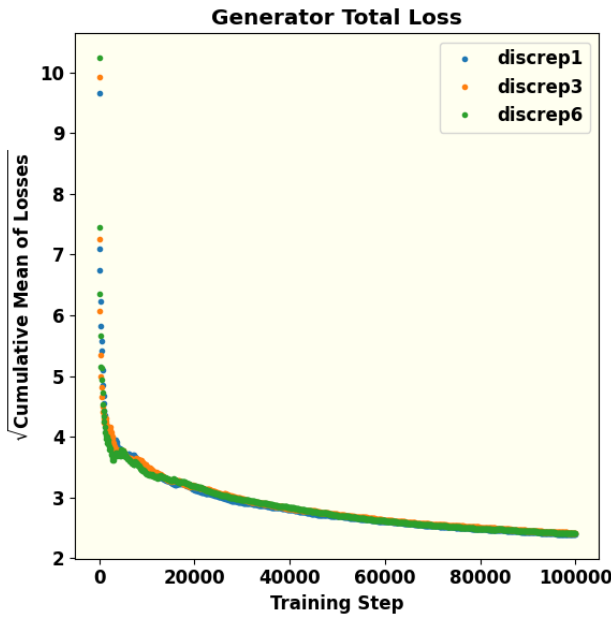
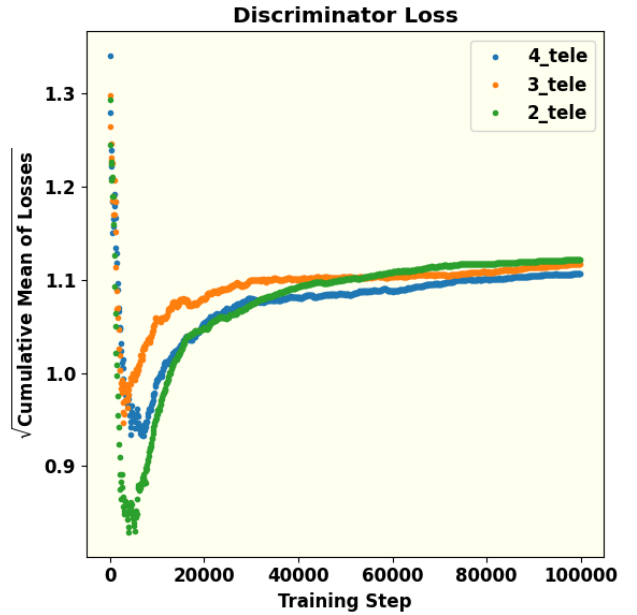
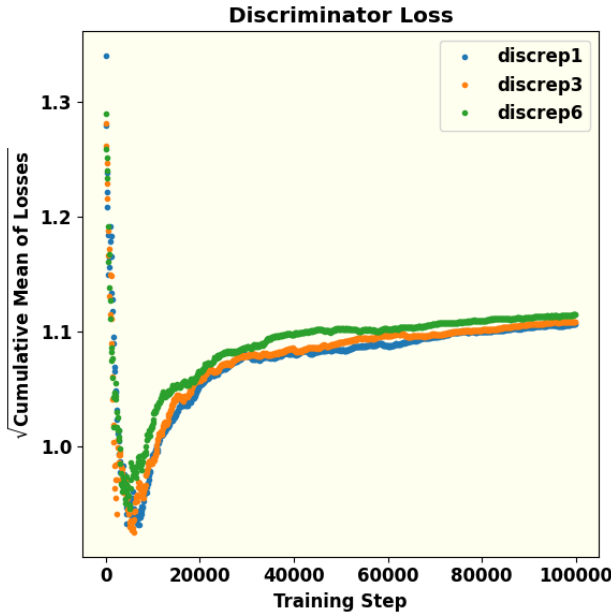


Figure 7. These figures show the effect of the ratio of episodes of Discriminator training per every episode of Generator training. This hyperparameter is termed Discriminator repetition or (discrep) in the figures. The square root of the cumulative mean of the losses are plotted against the training steps for 3 values of this ratio. Understandably, this ratio has a higher impact on the Discriminator loss than the Generator loss. Equal number of episodes of training produces minimum cumulative loss of the Discriminator. The dip in the Discriminator loss during the initial phases of its training can be interpreted as its early success in detecting “fake” (or generated) images because of a poorly trained Generator. With gradual training of the Generator, the success rate of the Discriminator decreases and eventually approaches saturation with equal probability of being successful in telling “fake” from real. The continual decrease and eventual saturation of the Generator loss is a result of its training to generate better images with increasing number of steps.
 DOI: [10.5281/zenodo.1759867](https://doi.org/10.5281/zenodo.1759867)

Figure 8. The square root of cumulative mean of Discriminator and Generator loss for different numbers of telescopes. The number of telescopes is also another hyperparameter that has significant impact on the model performance. If there are only two telescopes, both Discriminator and Generator are not trained smoothly. The result of four telescopes is a lot better because the cumulative mean of loss functions is smaller compare to other parameters. For the same reasons as explained in Fig.(7), we observe initial dip and eventual saturation of the Discriminator loss and continual decrease and eventual saturation of the Generator loss with training steps.

527 During the training, the total Generator Loss function
 528 L_G including the L_1 loss defined in eq.(13) that is
 529 minimized is given by

$$530 \quad L_G = -\mathbb{E}_{z \sim p_z(z)} [\log D(G(z | y) | y)] \\ + \lambda \mathbb{E}_{x \sim p_{\text{data}}, z \sim p_z(z)} [\|x - G(z | y)\|_1]. \quad (15)$$

531 Here,

- 532 • x denotes a real data sample (e.g. the “ground-
 533 truth” image; here, the synthetically generated
 534 fast rotator image) corresponding to condition y ,
 535 the simulated II observation data.
- 536 • z is a random latent vector drawn from the prior
 $p_z(z)$.
- 538 • $G(z | y)$ is the generator output (the reconstructed
 539 / synthesized image) given z and condition y .
- 540 • $D(\cdot | y)$ is the discriminator’s estimate (probabil-
 541 ity) that its input is “real,” given the same condi-
 542 tion y .
- 543 • λ is a hyperparameter controlling the trade-off be-
 544 tween adversarial realism and pixel-wise fidelity
 545 (typical values depend on the problem, e.g. in
 546 pix2pix, $\lambda = 100$).

547 4.2. Discriminator

548 The Discriminator is tasked with classifying the im-
 549 ages produced by the Generator as either real or fake.
 550 It takes a real image from the dataset (often referred
 551 to as the target image for the Generator) and provides
 552 feedback to guide the Generator toward producing more
 553 accurate images. In this work, the PatchGAN model
 554 (?) is employed as the Discriminator. Unlike a tradi-
 555 tional global classifier, PatchGAN evaluates individual
 556 patches of the image, outputting a grid of predictions
 557 rather than a single scalar value. Each element in the
 558 grid corresponds to the “realness” of one patch of the
 559 image under examination of the Discriminator at a time.
 560 The final loss of the Discriminator is the average over
 561 all the patch responses. Evaluating the “realness” of
 562 the input image in terms of its constituent patches facil-
 563 itates capture of texture/ style and other high frequency
 564 components in the image. As compared to a global dis-
 565 criminator, it also reduces the number of parameters in
 566 the network thereby helping reduce computation cost.
 567 It also works on images with arbitrary sizes.

568 Prior to the down-sampling of data using PatchGAN,
 569 each input image is preprocessed with application of
 570 Zero Padding followed by batch normalization. The pur-
 571 pose of Zero Padding is to prevent the loss of spatial
 572 information and to facilitate the extraction of deeper

573 features from the down-sampled output. Batch normal-
 574 ization is required to stabilize the learning (loss mini-
 575 mization) process. PatchGAN then reduces the spatial
 576 dimensions of the images to extract localized features,
 577 ensuring the model focuses on smaller regions. In this
 578 down-sampling stage, a leaky version of the Rectified
 579 Linear Unit (LeakyReLU) is applied in the convolutional
 580 layers, similar to the approach used in the Generator.
 581 The probability $D(\cdot | y)$ that the patch of the input im-
 582 age represented by \cdot is “real” is evaluated through this
 583 process. The loss function D of the full input image is
 584 obtained by averaging over all the patch responses.

585 The Discriminator Loss function L_D that is optimized
 586 during the training process is given by

$$587 \quad L_D = -\mathbb{E}_{x \sim p_{\text{data}}(x | y)} [\log D(x | y)] \\ - \mathbb{E}_{z \sim p_z(z)} [\log (1 - D(G(z | y) | y))] \quad (16)$$

588 where the arguments of the D and G functions are as
 589 noted in the text following eq.(15). This loss is composed
 590 of two parts: one that assesses how accurately it iden-
 591 tifies fake images (by comparing predictions to a target
 592 value of 0) and the other that measures how accurately
 593 the Discriminator identifies real images (by comparing
 594 predictions to a target value of 1).

595 The training procedure of these two components of
 596 the cGAN model can be outlined as follows:

- 597 • The discriminator D is updated by minimizing
 L_D , keeping G fixed (so that D becomes better
 599 at distinguishing real vs generated images).
- 600 • The generator G is updated by minimizing L_G ,
 601 keeping D fixed, thus pushing G to generate im-
 602 ages that are (a) judged “real” by D , and (b) close
 603 (in pixel-wise sense) to the ground-truth x .

604 5. NETWORK PARAMETERS

605 An appropriate cGAN architecture along with a set of
 606 hyperparameters was optimized by tuning. The objec-
 607 tive of the model, as already mentioned, was to learn to
 608 faithfully reproduce a set of sky-images of fast rotators
 609 subject to the condition that those images are consistent
 610 with their simulated II observation data. We discuss
 611 below the architecture and the hyperparameters of the
 612 cGAN model used for this task. Given the adversarial
 613 nature of GANs, where the Generator and Discrimina-
 614 tor engage in a minimax game, careful tuning of key
 615 parameters is critical to ensure that both networks are
 616 well-balanced for effective training.

617 5.1. Data Preparation

618 First, we generate synthetic images of rapidly rotating
 619 stars by modelling them as oblate spheroids with vary-
 620 ing radii and oblateness parameters between 0.5 and 1.

To incorporate the effect of gravity darkening, we also consider different viewing angles and assume a linear dependence on the declination angle of each point on the stellar surface. The traced ellipses result from integrating over the source's hour angle.

Next, Salt and Pepper noise is introduced into these images; usually this is done at the rate of 0.5% of the number of pixels in the image. Then, the images are resized and their mean is subtracted. A two-dimensional Fast Fourier Transform, along with a Fourier shift, is applied, yielding a complex number for each pixel. Since II does not measure phase, the absolute value is calculated.

Next, sampling of the interferometric plane is introduced via pixel-wise multiplication of the absolute-valued Fourier-transformed image (left panel of Fig. 4) and the baseline tracks of (Fig. 2) generated by the four IACTs due to Earth rotation during the II observation. The result is a map in the Fourier plane featuring several ellipses, which is also referred to as the sparse sampling map (right panel of fig. 4). This map represents the sparse sampling of the signal space corresponding to the source (Fig. 3) observed with four telescopes (Fig. 1). In essence, the right panel of fig. 4 represents the result of simulated II observation of the fictitious fast-rotator illustrated in fig. 3.

Finally, we normalize the pixel values and convert them to 8-bit integers, producing an image that encodes the sparsely sampled, phase-free visibility measured by II. The image of the corresponding simulated (fictitious) star, which serves as the “ground truth” is processed identically to avoid any bias. These two images are merged side-by-side into a single image (as shown in Fig. 5). The dataset thus created is split into three parts in the proportions of 80% for training, 10% for validation, and 10% as the test set. This partition of the full dataset is indicated in the Fig. 6. In the following, we refer to these three parts as the Training Set, the Validation Set and the Testing Set respectively.

5.2. GAN Architecture

The GAN architecture used in this work is a Pix2Pix cGAN, which uses an image-to-image translation strategy with both the ground truth and the condition being images. Originally introduced by Isola et al. ?, this architecture is specifically suitable for image processing and reconstruction objectives. For instance, the TensorFlow tutorials⁶ demonstrate its application to a dataset of architectural facades. This architecture has been adapted for the phase retrieval problem at hand here. The network is implemented using the Tensor-

Flow library (?), calculations are performed with scipy (?), and plots are generated with matplotlib (?).

5.3. Hyperparameter Tuning

The cGAN model architecture used in this work employs several hyper-parameters, which are explained briefly below (for a more in-depth discussion, see ?).

The learning rate (lr) of the optimizer determines how much the model updates its parameters with each iteration. A learning rate that is too small may lead to underfitting, while one that is too large can render the model unstable. Therefore, selecting an appropriate learning rate is crucial (?). A canonical choice in Pix2Pix and other GAN models is $lr = 2 \times 10^{-4}$. In our case too, we found this choice to be appropriate.

The kernel size refers to the dimensions of the convolutional kernel used in the network, determining how many pixels are combined to produce a new pixel. A larger kernel size can capture features spanning several pixels, but it may also incorporate unrelated features. Small kernel sizes are preferable in cases where target images finer details or high spatial frequency features. Since the “ground truth” target images in our case have longer scale gravity darkening features, we have opted for the more canonical choice of kernel size being 5.

The amount of noise is controlled by two parameters, “alpha” and “beta”, which indicate the percentage of pixels altered to either white or black, hence the term Salt and Pepper noise. Here, “alpha” is applied to the real image, while “beta” is applied to the generated image. Different ratios (“alpha/beta”) can lead to varying model performance; however, our results indicate that distinct noise rates do not significantly affect the loss functions.

The batch size defines the number of images processed simultaneously by the network. Smaller batch sizes have been observed to improve generalization (?). However, because a larger batch size significantly increases training time, a batch size of 1 is used. Besides, in Pix2Pix cGAN implementations found in literature this choice is found to be often preferred.

Buffer size of a Pix2Pix GAN refers to a small memory of image pool of previously generated images. They are occasionally fed to the Discriminator in place of the freshly generated ones. This strategy of mixing old and new fakes mitigates the risk of mode collapse wherein the Discriminator tends to map all or large number of generated images to only one or a few real “ground truth” image(s). We have chosen a fairly large buffer size (=1400) to protect the model against mode collapse.

In the training of GANs, one often-followed strategy to potentially boost performance is to give the Discrim-

⁶ <https://www.tensorflow.org/tutorials/generative/pix2pix>

inimator an advantage by increasing its number of training epochs before returning to the Generator's training. This hyperparameter is referred to as the Discriminator repetition (as seen in Table 1). While this can lower the Discriminator loss, as shown in Fig. 7, it also increases training time. In training our model, we did not notice any significant advantage derived from this strategy. Since the generated images did not noticeably improve with additional Discriminator training, we adopted the strategy of training both the networks with equal preference (Discriminator repetition = 1).

One domain specific hyperparameter of the cGAN model presented here is the Number of Telescopes N_T . The degree of sparse sampling of the intensity interferometric (II) image plane can be varied to provide the model with access to more number of active (non-zero) pixels. Point to note here, is that the coverage of the Fourier interferometric plane (number of active pixels in the II image) scales with available number of baselines, and the latter scales quadratically with the number of telescopes. Fig. 8 shows the loss functions for different numbers of telescopes. There is a significant disparity in performance of the model: at the “Nash point”, both the loss functions are minimized for the case of four telescopes. Overall, the degree of sparse sampling appears to have the most pronounced effect of all the hyperparameters.

The hyperparameter Output Channels refers to the number of channels in the generator output (e.g., 1 for grayscale, 3 for RGB). It is worthwhile to recall that the cGAN model constructed in this work is trained on “ground truth” target images and the simulated II data, both in grey scales as seen in Fig. 5. It is natural that the output of this model will be in grey scales only. Therefore the value of this hyperparameter is set to 1. The choice of hyperparameter λ has been commented upon earlier.

An optimized set of hyperparameters is selected through an iterative process of training and validation. For a tentatively chosen set of the hyperparameters, the model is trained using the Training Set until the both the Discriminator and the Generator loss functions are minimized. This model, thus trained along with its model parameters, is then passed through validation using the Validation Set. This cycle of training and validation is iterated till an optimal set of hyperparameters is arrived at. During each epoch of training of the model, both the Discriminator and the Generator networks are trained for 100,000 steps. Plots of the “Discriminator Loss” function and the “Generator Total Loss” function presented in Fig. 7 and Fig. 8 represent the results of this training for two of the hyperparam-

ters, namely, the Discriminator repetition (“discrep”, in short) and the Number of telescopes, respectively. Obviously, the most compute-intensive part of this process is that of the training of the Model. The results of training and validation presented in this work were carried out on a CPU using two nodes, each with 96 threads and the entire process of training and validation required approximately 20 hours on the machine employed for this work. This iterative process of training and validation of the Model is represented schematically in the Fig. 6. The chosen optimal set of hyperparameters is presented in the table Table-1. This optimized and trained Model

Table 1. Selected hyperparameters used for training the model.

Hyperparameter	Value
Learning rate	2e-4
Kernel size	5
Alpha/Beta	1
Batch size	1
Buffer Size	1400
Discriminator repetition	1
Number of Telescope	4
Output Channels	1
Lambda	100

is then subjected to testing and evaluation using the Testing Set. The results of this testing and evaluation is presented in the following section.

The Pix2Picx cGAN architecture along with the choice of the values of the hyperparameters mentioned in the Table -1 and used in the implementation of this architecture constitutes the cGAN model (hereinafter referred to as “the GAN Model” or simply “the Model”).

6. IMAGE RECONSTRUCTION: RESULTS AND EVALUATION

In this section, we examine the performance of the GAN Model whose architecture and choice of hyperparameters have been discussed above. We subject the trained Model to the task of phase retrieval and image reconstruction on the Testing Dataset.

6.1. Visual Evaluation of Images Predicted by the Model

Fig. ?? demonstrates the success of the trained Model in reconstructing the images of a sample of the fictitious fast-rotators drawn from the Testing Set.

The four panels from left to right in each row of Fig. ?? represent the following:

- The left panel represents the sparse II pattern obtained by the simulated observation using the four

IACTs illustrated in Fig. 1. As explained earlier, this image acts as part of the input, namely its “condition” part. This image acts as the condition that the sky-images of the star generated by the Generator must conform to.

- The second panel from left displays the real image, or ground truth target image, which the Discriminator loss function uses to distinguish from the images generated by the Generator.
- The third panel from left presents the reconstructed (or predicted) image corresponding to the ground truth (second panel) and generated by the trained Model. The similarity of these two images indicates the success of the Model in its stated objective of image reconstruction.
- The right panel shows the residuals between the ground truth target image and the predicted image in the interferometric plane. The small values are indicative of the success of training the Model.

The predicted images and the residuals presented in the third and the fourth columns (from left) of Fig. ?? show encouraging results, conveying visual information about the source’s size, shape, and brightness distribution across its surface fairly accurately. This has been achieved on the basis of the input provided by II observation using only six baselines. Arguably, further improvements can be achieved by increasing the number of telescopes to enhance the coverage of the (u, v) plane. A closer examination of this proposition might be able to contribute to the design and instrumentation aspects in the existing and upcoming CTAO.

6.2. Evaluation of the Model using Moments

The reconstructed images are visually compelling, demonstrating the Model’s effectiveness in using II to reconstruct images. However, visual assessment alone is insufficient; statistical evaluation of the generated images in comparison with the ground truth images is necessary to validate the results. We present here the results of our calculation and comparison of the moments of distribution pixel brightness in the target “Ground Truth” images and the “Predicted” images.

Image moments capture key properties of the reconstructed objects, such as shape, size, and intensity distribution, by quantifying features like position, orientation, and brightness distribution. By comparing the moments of the Model-generated images with those of the ground truth, we can objectively assess the consistency and accuracy of the reconstruction. This approach provides a reliable framework for evaluating reconstruction

quality, as image moments can reveal subtle differences in geometric and intensity properties that might not be apparent through visual inspection alone.

The raw moment M_{ij} of an image is defined as (?)

$$M_{ij} = \sum_x \sum_y x^i y^j I(x, y) \quad (17)$$

where $I(x, y)$ represents the intensity at pixel (x, y) . The zeroth order raw moment, or monopole, represents the total intensity of an image. It is computed by summing all pixel values across the image, yielding an overall intensity measure. In this context, analyzing the monopole provides the total pixel brightness of the images of the fictitious stars. According to Eq. (17), the monopole of an image is calculated as:

$$M_{00} = \sum_x \sum_y I(x, y). \quad (18)$$

An ideally trained Model should predict the overall pixel brightness of the generated images to be in the same range of values, if not equal to those of the ground truth images. The left panel of Fig. 10 displays the monopole values for 100 reconstructed images. The plot reveals a broad agreement in the overall intensity of the ground truth targets and the predicted (generated) images. However, a slightly higher brightness of reconstructed images in the intermediate range of brightness is evident. This could, perhaps, be mitigated by tuning the Batch Size hyperparameter.

While the monopole effectively represents the total brightness, it does not provide information about the position, shape, size, or detailed brightness distribution of the fast-rotating stars. For these aspects, higher-order moments are necessary.

The first order raw moments normalized by the respective monopole moments of the images given by

$$x_c = \frac{M_{10}}{M_{00}} = \frac{\sum_{x,y} x \cdot I(x, y)}{\sum_{x,y} I(x, y)}$$

$$y_c = \frac{M_{01}}{M_{00}} = \frac{\sum_{x,y} y \cdot I(x, y)}{\sum_{x,y} I(x, y)} \quad (19)$$

represent the centroids (x_c, y_c) of the pixel brightness distribution of the images. An ideally trained GAN model should produce the centroids of the target and predicted images within a small range of pixels. A larger range would imply a low fidelity in learning the brightness distribution of ground truth images. The middle and right panels of Fig. 10 compare the centroids (x_c, y_c) of 100 predicted images with their corresponding ground truths respectively. We notice that the coordinates of

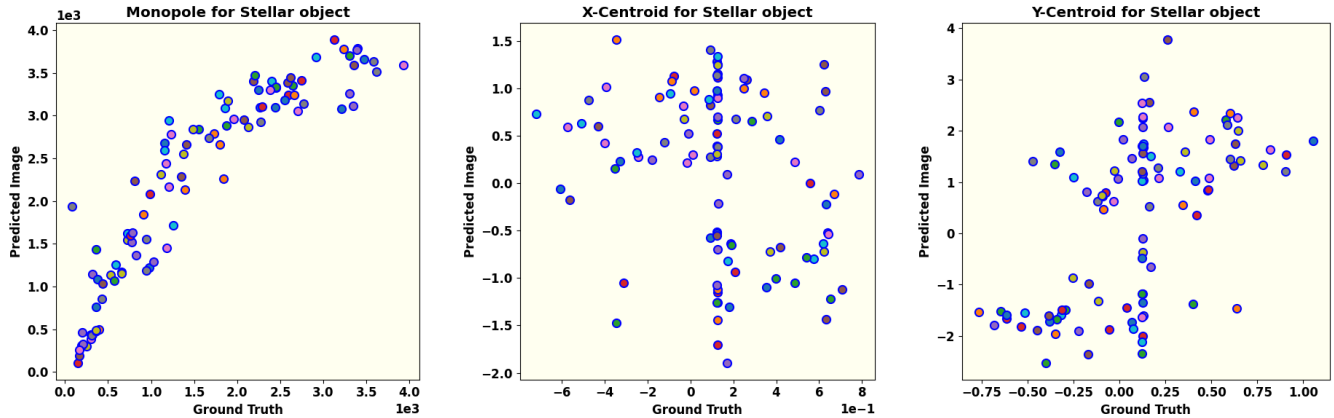


Figure 10. This set of figures shows comparisons of the monopole, and the coordinates of the centroids (x_c, y_c) of the pixel brightness distribution of the ground truth images and the corresponding images predicted (generated) by the trained model. The monopole moment of the images represents the overall pixel brightness of the images. The values, as expected of a trained Model, not only lie in same range, but lie close to the diagonal and show an approximate equality. The centroids of both the ground truth images and the predicted images lie within small ranges of pixel values as should be expected of an ideally trained model. Please see the relevant text for detailed comments.

the centroids of ground truth images are spread across a range of 2 pixels whereas the those of the predicted images are spread across a span of 4 pixels along x -axis and 7 pixels along y -axis. This clustering of centroids within a small scale range across all results indicates that the reconstructed images represent the spatial distribution of brightness of predicted and ground truth images fairly accurately.

Furthermore, these calculated centroids are instrumental in analyzing the shape, size, and brightness distribution of the stars using higher-order image moments. To this end, the central moment of an image is calculated according to:

$$\mu_{pq} = \frac{1}{M_{00}} \sum_x \sum_y (x - x_c)^p (y - y_c)^q I(x, y). \quad (20)$$

The sum of p and q defines the order of the central moment.

The second order central moment of the brightness distribution of the images is analogous to the moment of inertia of a mass distribution. Fig. 11 presents the comparison of second-order central moments ($\mu_{11}, \mu_{20}, \mu_{02}$), which are used to study the structure of a fast-rotating star along the line of sight (as explained in the upcoming subsection). All three plots demonstrate an approximate equality among these moments, similar to the monopole, thereby confirming the success of applying the Model to reconstruct images with II. The small scatter in the moments of the predicted images indicates robust learning of the Model without over-fitting.

The third-order central moments ($\mu_{30}, \mu_{03}, \mu_{21}, \mu_{12}$) of the images quantify the degree and direction of asymmetry of the brightness distribution around their respective

centroids. Fig. ?? presents a comparison of all third-order moments for both the ground truth and the reconstructed image. All the four panels show a low skewness in the brightness distribution of the ground truth images. The skewness of the predicted images along the y -axis is dominated by one outlier as seen in the values of μ_{03} and μ_{12} . However, the approximately uniform distribution of skewness of the predicted images along the x -axis, with a few outliers though, as seen in the values of μ_{30} and μ_{21} suggests that this feature in the ground truth images has been picked up fairly well during the training of the Model.

6.3. The reconstructed Parameters for object

The centroids (x_c, y_c) indicate only the center of the star and its spatial location in the image. In contrast, the second-order central moments determine the orientation, semi-major axis, and eccentricity relative to the source's center (?). These moment-based parameters fully describe the two-dimensional ellipse that fits the image data.

The orientation of a fast-rotating star along the line of sight is defined in terms of second-order central moments as

$$\theta = \frac{1}{2} \arctan \left(\frac{2\mu_{11}}{\mu_{20} - \mu_{02}} \right). \quad (21)$$

The semi-major and semi-minor axes of the stellar object are computed using the second-order central moments and are denoted as a and b , respectively.

$$a = 2\sqrt{mp + \delta} \\ b = 2\sqrt{mp - \delta} \quad (22)$$

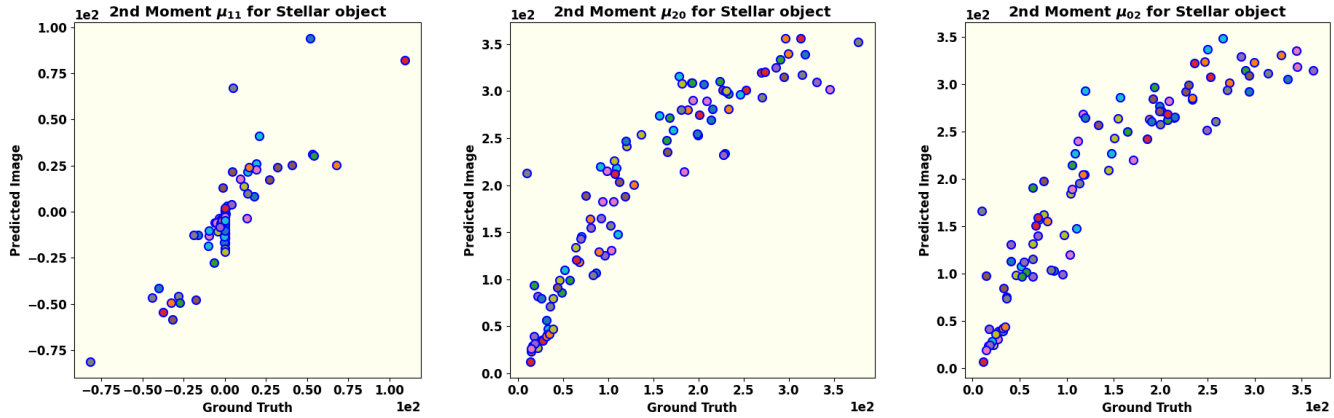


Figure 11. The second order central moment of the brightness distribution of the images is analogous to the moment of inertia of a mass distribution. The panels of this figure show the comparison of the second order moments (μ_{11} , μ_{20} , and μ_{02}) of the predicted images vs. the ground truth images from left to right respectively. Approximate equality of these moments is evident. The small scatter in the moments of the predicted images is indicative of a balanced training of the Model.

where,

$$mp = \frac{\mu_{20} + \mu_{02}}{2} \quad (23)$$

and

$$\delta = \frac{\sqrt{4\mu_{11}^2 + (\mu_{20} - \mu_{02})^2}}{2}. \quad (24)$$

Using the calculated axis values, the eccentricity of the fast-rotating star is determined as:

$$e = \sqrt{1 - a/b}. \quad (25)$$

Eqs. 21-25 describe the elliptical nature of the stellar object (in this case, a fast-rotating star) and provide information on its shape and size, depending on the computed values. In contrast, the brightness distribution is characterized by skewness, which is quantified using third and higher-order moments.

7. CONCLUSION

Intensity Interferometry (II) is re-emerging as a promising technique to overcome the challenges of very long baseline interferometry in the optical wavelength range. However, compared to radio-interferometry, optical interferometry faces a major hurdle: photon correlation captures only the magnitude of the interferometric signal, resulting in a loss of phase information.

This work addresses the challenge of phase retrieval in II using a machine-learning technique, specifically a conditional Generative Adversarial Network (cGAN). Our study demonstrates that the size, shape and brightness distribution of fast rotating stars can be recovered by a Pix2Pix cGAN model trained on the combined input of the sky-image of known sources along with their respective II data. In this training the sky-image acts as the real “ground truth” and the II data acts as the

“condition”. The Discriminator of our Model is trained to efficiently distinguish between the real images and fake (generated) images based on the “ground truth” images and the respective II data as the condition. The Generator is trained to generate progressively realistic images which are also consistent with the condition of the II data. The evaluation of the trained Model is then carried out by comparison of image moments of ground truth images and generated images. Specifically, the monopole, second, and third-order moments are compared. The results support the effectiveness of cGAN in achieving the stated objective.

While the results of this study highlight the significant potential of machine learning, and in particular the applicability of cGAN, for image reconstruction in II, several aspects require further refinement. First, an important factor in the reconstruction process is the extent of Fourier plane coverage, which depends on the number of available telescopes and the total observing time. The reasonable success of this piece of work suggests that a network of higher number of telescopes providing higher number of baselines and greater coverage of the (u, v) plane signal, would play a critical role in projects of image reconstruction of more complicated stellar systems can be undertaken. Future work might explore different observatory layouts to assess their impact on image reconstruction quality. Second, detector efficiencies, which impact the signal-to-noise ratio (SNR) of actual observational data, have not yet been incorporated; addressing these factors will be crucial for more accurate SNR estimation. Third, exploring and comparing alternative methods for image generation could reveal approaches that outperform cGAN in reconstructing stellar images with II. Fourth, experimenting with different loss functions could provide additional insights into the recon-

1028 struction quality. Although further testing is needed to
1029 refine the GAN and enhance its robustness and reliabil-
1030 ity, our findings suggest that machine learning is a
1031 promising approach for phase reconstruction in II.

1032 ACKNOWLEDGEMENTS

1033 **Acknowledgment:** One of the authors (SS) gratefully
1034 acknowledges the computing facilities and the local hos-
1035 pitality extended to him by the Inter-University Centre
1036 for Astronomy and Astrophysics (IUCAA), Pune, In-
1037 dia under its Visiting Associate Programme during the
1038 preparation and finalization of this manuscript.